Dalton Transactions

RSC Publishing

PAPER

View Article Online
View Journal

Bi-functional properties of Fe_3O_4@YPO_4:Eu hybrid nanoparticles: hyperthermia application†

Cite this: DOI: 10.1039/c2dt32508j

A. I. Prasad,[a] A. K. Parchur,[b] R. R. Juluri,[c] N. Jadhav,[d] B. N. Pandey,[d] R. S. Ningthoujam*[a] and R. K. Vatsa[a]

Magnetic nanoparticles based hyperthermia therapy is a possible low cost and effective technique for killing cancer tissues in the human body. Fe_3O_4 and Fe_3O_4@YPO_4:5Eu hybrid magnetic nanoparticles are prepared by co-precipitation method and their average particle sizes are found to be ~10 and 25 nm, respectively. The particles are spherical, non-agglomerated and highly dispersible in water. The crystallinity of as-prepared YPO_4:5Eu sample is more than Fe_3O_4@YPO_4:5Eu hybrid magnetic nanoparticles. The chemical bonds interaction between Fe_3O_4 and YPO_4:5Eu is confirmed through Fe···O–P. The magnetization of hybrid nanocomposite shows magnetization M_s = 11.1 emu g^{-1} with zero coercivity (measured at 2×10^{-4} Oe) at room temperature indicating superparamagnetic behaviour. They attain hyperthermia temperature (~42 °C) under AC magnetic field showing characteristic induction heating of the prepared nanohybrid and they will be potential material for biological application. Samples produce the red emission peaks at 618 nm and 695 nm, which are in range of biological window. The quantum yield of YPO_4:5Eu sample is found to be 12%. Eu^{3+} present on surface and core could be distinguished from luminescence decay study. Very high specific absorption rate up to 100 W g^{-1} could be achieved. The intracellular uptake of nanocomposites is found in mouse fibrosarcoma (Wehi 164) tumor cells by Prussian blue staining.

Received 21st October 2012,
Accepted 21st December 2012

DOI: 10.1039/c2dt32508j

www.rsc.org/dalton

I. Introduction

Nanomaterials exhibit different physical and chemical properties as compared to bulk due to effects from small particle size, quantum size (in semiconductor) and high surface area.[1–7] Nowadays, bi-functional composites (BFC) in nanosize regime are more attractive because of more functionality in terms of properties and simple, reduction in cost.[8–12] BFC having both magnetic as well as optical properties have been of great interest in recent years.[13–19] YPO_4 is used as host material for many lanthanide activators.[20–23] Amongst lanthanide activators, Eu^{3+} gives high luminescence peaks at 615 and 695 nm (red) and it is sensitive to the local environment because Eu^{3+} ions occupy Y^{3+} sites, where EuO_8 is highly asymmetric (D_{2d}).[24,25] The red emission is included to the biological window. The red emission can be produced by either 395 or 465 nm excitation. Thus, this material is used in many display applications. When the particle size of a material decreases to the nano range, its importance increases in many applications.[26–29] In particular, these red emitter nanoparticles (RENPs) are used in many life science applications as luminescence probes/labels.[30]

On the other hand, Fe_3O_4 material has been used in many applications as a transformer and for data storage.[31–36] Bulk Fe_3O_4 material shows interesting intrinsic ferromagnetic property (saturation magnetization (M_s = 92 emu g^{-1}), coercivity (H_c = 323 Oe)) at room temperature and high Curie temperature (T_c = 585 °C).[34–37] When particle size decreases to nanosize, this material is useful in many applications such as biosensor, contrasting agent in magnetic resonance (MR) imaging, localizer in therapeutic hyperthermia, magnet targeted drug delivery system, gene carrier, catalyst, sensors, biological separation and water purification, *etc*.[31–36] There have been various methods developed for preparation of Fe_3O_4 like that of co-precipitation, hydrolyzation, micro emulsion *etc.* Out of which, co-precipitation is most widely used as it is simple and fast.[14] All commercially available Fe_3O_4 based contrast agents have been synthesised only by co-precipitation

[a]*Chemistry Division, Bhabha Atomic Research Centre, Mumbai-400 085, India. E-mail: rsn@barc.gov.in, nraghu_mani@yahoo.co.in; Fax: +91-22-25505151; Tel: +91-22-25592321*
[b]*Department of Physics, Banaras Hindu University, Varanasi-221 005, India*
[c]*Institute of Physics, Sachivalaya Marg, Bhubaneswar-751 005, India*
[d]*Radiation Biology and Health Sciences Division, Bhabha Atomic Research Centre, Mumbai-400 085, India*

†Electronic supplementary information (ESI) available: For schematic representation of the processing steps used in synthesis; change in peak position of (200) plane with and without 5 at% Eu^{3+} doping in YPO_4 host in XRD patterns; comparison of peaks corresponding to PO_4 group in FTIR spectra of YPO_4:Eu and Fe_3O_4@YPO_4:5Eu nanoparticles. See DOI: 10.1039/c2dt32508j

method using NH_4OH. Ammonia solution holds superiority in comparison with NaOH. Addition of NaOH increases the pH of the solution instantly thus causing the formation of bigger particles, whereas in the case of NH_4OH the increase in pH is slow thus helping to form nano sized particles. Such magnetic nanoparticles are superparamagnetic at room temperature, *i.e.*, H_c = 0 Oe and M_s = 50–60 emu g^{-1}.[37] Due to this, these magnetic nanoparticles (MNPs) are paramagnetic, and thus, these are used as a significant contrasting agents in magnetic resonance imaging (MRI) and also in therapeutic applications showing ability to achieve the hyperthermia temperature (~42 °C). Both YPO_4 and Fe_3O_4 materials and even coated with ethylene glycol (EG) or polyethylene glycol (PEG) are biocompatible.[37,38]

Nowadays, a few systems exist for hyperthermia applications such as $La_{0.7}Sr_{0.3}O_3$ MNPs (half metallic and ferromagnetic properties) which can control heating temperature up to 50 °C at the presence of high current/magnetic field, high AC frequency and long duration of induction heating because of low Curie temperature (T_c ~ 50–80 °C). Whereas, Fe_3O_4 MNPs have high T_c ~ 585 °C. Because of this, heating temperature can attain up to 200–400 °C, which is undesirable for therapy.

When RENPs and MNPs are combined, they have many interesting bi-functionality properties (luminescence and magnetic properties). These bi-functional materials show importance in biomedical research clinical diagnosis and therapy. The magneto-luminescent nanocomposites gain significance since its magnetization can be controlled with real time visualization of its luminescence. The use of bi-functional composites improves diagnostic effectiveness and reduces side effects.[39]

In this work, we have successfully synthesised Fe_3O_4@YPO_4:5Eu nanocomposites by first preparing Fe_3O_4 by co-precipitation and YPO_4:5Eu over Fe_3O_4 by direct precipitation. Here surface of Fe_3O_4 is coated with PEG which can form a covalent bond with the YPO_4:5Eu precipitated thus forming Fe_3O_4@YPO_4:5Eu magneto-luminescence nano-platform. The synthesised powder is characterised using many techniques. The quantum yield has been carried out. Samples are dispersible in polar medium. The study of its heating ability was performed to determine its hyperthermia behaviour. Their specific absorption rates are calculated at different magnetic fields at a particular radiofrequency. The intracellular uptake of nanocomposites is studied in mouse fibrosarcoma (Wehi 164) tumor cells by Prussian blue staining. High intracellular uptake by tumor cells is a pre-requisite for their biomedical applications.

II. Experimental

A. Reagents and chemicals

Polyethylene glycol (PEG 6000, 99.99%), Y_2O_3 (99.99%), $NH_4H_2PO_4$ (99.999%) and Eu_2O_3 (99.99%) from Sigma-Aldrich, $FeCl_3{\cdot}6H_2O$ (99%) and $FeSO_4{\cdot}7H_2O$ (99.5%) from Merck, paraformaldehyde (96%) and NH_4OH solution (12 M) from S. D. fine chemicals were purchased and used as starting materials without further purification.

B. Preparation of nanoparticles

(i) Preparation of Fe_3O_4 magnetic nanoparticles. Fe_3O_4 magnetic nanoparticles were prepared by a co-precipitation method using the following steps:

Step (1): 1.0 g of $FeSO_4{\cdot}7H_2O$ and 1.945 g of $FeCl_3{\cdot}6H_2O$ (1 : 2 molar ratios) were mixed with 50 ml of deionised water. To the resulting solution, concentrated HCl acid (11 N) was added drop wise under continuous stirring with glass rod in a beaker until a clear pale yellow colour solution was formed. To this solution, 30 ml of 12 M NH_4OH was added drop wise with constant stirring and a black precipitate was obtained, and it was kept for 24 hours for complete precipitation. The obtained Fe_3O_4 was washed 5 times with deionised water to remove excess of NH_3. A strong magnet of 2.5 kOe was placed to the base of the glass beaker containing Fe_3O_4 and supernatant liquid. Fe_3O_4 was attached to the magnet and the supernatant liquid was removed with a help of the micropipette. The reaction can be represented as follows:

$$Fe^{2+} + 2Fe^{3+} + 8OH^- \rightarrow Fe_3O_4 + 4H_2O$$

Step (2): The nanoparticles prepared in step (1) were transferred in to another beaker containing 10 ml of distilled water and 5 g of PEG and it was allowed ultrasonication for 1 h. In this way the surface of Fe_3O_4-MN was coated with PEG and prepared sample was dispersible in water.

Then, as-prepared sample (Fe_3O_4) was washed twice with acetone (10 ml) under centrifugation. Now, dry powder was obtained.

(ii) Preparation of YPO_4:5Eu luminescence nanoparticles. 5 at% Eu^{3+} doped YPO_4 luminescence nanoparticles (YPO_4:5Eu) were prepared by the following procedure. 1.543 g of Y_2O_3 and 0.127 g of Eu_2O_3 were dissolved in 2 ml of concentrated HCl acid (11.6 N). This solution was evaporated in order to remove excess HCl acid from the solution with alternate addition of 2 ml of deionised water followed by heating (80 °C). This evaporation process was repeated 4 times. 1.625 g of $H_4NH_2PO_4$, 2.5 g of PEG and 10 ml of deionised water were added to it. In order to make a clear solution, it was stirred and then heated at 120 °C for 2 h. A white precipitate was obtained and removed by centrifugation. The dried powder was obtained by washing with methanol (5 ml) and acetone (5 ml) under centrifugation.

(iii) Preparation of Fe_3O_4@YPO_4:5Eu hybrid nanoparticles. In the preparation of Fe_3O_4 coated with YPO_4:5Eu hybrid nanoparticles (Fe_3O_4@YPO_4:5Eu), 1.625 g Y_2O_3 and 0.127 g of Eu_2O_3 were dissolved in concentrated HCl acid (11.6 N) and the excess of acid was evaporated at 80 °C by alternate addition of distilled water and heating. To this solution, 5 g of PEG dissolved in 5 ml distilled water was added and allowed to

ultrasonicate for 30 min. This solution was added to PEG coated Fe_3O_4 (Step (1) of section B (i)). To the resulting mixture, 1.625 g of $H_4NH_2PO_4$ dissolved in 5 ml of deionised water was added drop wise and allowed to ultrasonicate for 1 h. The grey colour precipitate appeared. The resulting precipitate Fe_3O_4@YPO_4:5Eu) was collected by centrifugation. The dried powder was obtained after washing with 5 ml of methanol and 5 ml of acetone. Here, mole ratio of Fe_3O_4 to YPO_4:Eu is assumed as 1 : 4 based on starting precursors used. Schematic representation of the processing steps of synthesis of Fe_3O_4, YPO_4:5Eu and nanocomposite Fe_3O_4@YPO_4:5Eu is shown in Fig. S1 (see ESI†).

C. Characterization

Samples were characterized for their crystal structure and crystallite size with the help of Philips powder X-ray diffractometer (PW1729, Philips, Holland) with Ni filter and Cu-Kα radiation operated at 10 mA and 30 kV. The sample was spread over the slide by making it's paste with methanol and then dried off the methanol thus leaving behind a thin and uniform film which was examined to determine its crystallite size by X-ray diffraction on scanning rate of 2° min^{-1} in 2θ. Inter planar distance (d_{hkl}) of the plane (*hkl*) in sample was calculated by using Bragg's relation:

$$2d_{hkl} \sin\theta = \lambda \quad (1)$$

where λ is X-ray wavelength (*i.e.*, 1.5405 Å) and θ is Bragg's angle. The lattice parameter was calculated by using least square fitting programme of the diffraction peaks. The average sizes of the crystallites (t) were calculated using Scherrer relation on assumption of the crystallites to be spherical:

$$t = \frac{0.9\lambda}{\beta \cos\theta} \quad (2)$$

here β represents full width at half maximum (*FWHM*) of reflection/plane (*hkl*).

The interaction of the magnetic nanoparticles (Fe_3O_4) with the luminescence nanoparticles (YPO_4:5Eu) was studied using Fourier Transform Infrared (FTIR) spectroscopy technique (Bomem FTIR). The dried particles were used to make a thin transparent pellet with preheated KBr using a mechanical pellet making instrument which was used to record the spectra.

The particle morphology was studied using a transmission electron microscope (TEM) instrument (2000, FX, JEOL, Japan). Around 2 mg of the sample was dispersed in 1 ml of ethylene glycol and was subjected to ultrasonication for 30 min. From this resultant, a small aliquot of homogeneous and dispersed solution was put over the carbon coated copper grid. This copper grid with the sample solution was then evaporated to dryness and was later introduced to the TEM sample chamber to record TEM images. The HR-TEM (high resolution transmission electron microscope) images were obtained by using JEOL 2010 UHR TEM microscope.

The room temperature magnetizations of these samples were determined using Vibrating Sample Magnetometer (VSM). About 10–30 mg of sample was covered with Teflon and applied to VSM instrument.

The induction heating of the magnetic nanoparticles was studied using instrument Easy Heat 8310, Ambrell, UK. Induction coil had 4 turns having diameter of 6 cm. The applied frequency was 265 kHz and the provision of water circulation through their coils was provided in order to keep ambient temperature. 2–20 mg of samples suspended in 1 ml of deionised water was taken in 1.5 ml micro centrifuge tube and this was placed at centre of the coil without touching the walls. The sample was heated using current of 200, 300 and 400 A up to 10 min. The resultant magnetic field generated due to the applied current was calculated by making use of the following relation:[18]

$$H = \frac{1.257ni}{L} \text{ (in Oe)} \quad (3)$$

where H is the magnetic field, n, number of turns in coil, i, the applied current and L, diameter of turn in cm. The calculated values of the magnetic fields with respect to the applied currents of 200, 300 and 400 A were 168, 251 and 335 Oe (equivalent to 13, 20 and 27 kA m^{-1}), respectively. The temperature of the system, where the sample was kept in the centre of the coil was recorded using an optical temperature sensor (Photon R & D, Canada) with the accuracy of ±0.01 °C.

Estimation of iron content in the synthesized nanoparticles was carried out using (ICP-MS) inductively coupled plasma mass spectrometry. 10 mg of sample was dissolved in concentrated HCl.

Photoluminescence study of the sample was performed on Edinburgh Instrument FLS920 having 450 W xenon lamp and μs-Flash lamp (100 W). A thin film of samples was spread on a glass slide (~1 × 1 cm^2) with the help of methanol and dried before taking reading. For quantum yield measurements, Rhodamine G is used as reference.

Mouse fibrosarcoma (Wehi 164) cells were used to study the intracellular uptake of nanocomposites Fe_3O_4@YPO_4:5Eu by the tumor cells. Wehi 164 cells (1 × 10^6) were cultured overnight in Dulbecco's Modified Eagle Medium (DMEM; GIBCO, Invitrogen, Carlbad, CA, USA) supplemented with 10% fetal calf serum (FCS; Himedia Laboratories) and antibiotics (100 U ml^{-1} penicillin and 100 μg ml^{-1} streptomycin) in a humidified atmosphere of 5% CO_2 at 37 °C. The cells were then treated with 0.5 mg ml^{-1} nanocomposites for 4 h. Thereafter, cells were washed twice with PBS (phosphate buffered saline) and followed by fixing in 4% paraformaldehyde at 4 °C for 30 min. The cells were again washed with PBS twice, followed by staining the nanocomposites using Prussian blue iron staining kit (Polysciences, Inc., Germany). The nanocomposites were stained blue in colour and the cells were counterstained red with 1% nuclear fast red solution. Later, the cells were destained with PBS and visualized by bright field microscopy at 40× magnification.

III. Basic concept on the heat-generation from magnetic fluids under AC magnetic field or induction coil

Dispersed magnetic nanoparticles are free to move (that is because of Brownian motion). For considerably small sized particles there are two types of relaxations namely Brownian relaxation due to particle rotation and Néel's relaxation due to magnetic moment rotation. Brownian relaxation applies to all particles whereas Néel's relaxation is effective only on superparamagnetic nanoparticles. Brownian relaxation is given as:[18]

$$\tau_B = \frac{4\pi\eta {r_h}^3}{k_B T} \quad (4)$$

where η is dynamic viscosity of carrier fluid, r_h, hydrodynamic radius which is defined as the sum of core radius (r_c) and the surfactant coating (δ) on magnetic nanoparticles.

On the other hand Néel relaxation is represented as:[18]

$$\tau_N = \tau_0 e^{\Delta E/k_B T} = \tau_0 e^{KV/k_B T} \quad (5)$$

where τ_0 is of the order 10^{-9} s and ΔE, the anisotropic energy barrier which can be defined as the product of anisotropic energy constant (K) and volume (V), k_B, Boltzmann's constant and T, the temperature. Néels relaxation is fast for the small particles. When small particles are dispersed, the particle spin relaxation of the nanoparticles gets accelerated.

It should be noted that *DC* applied magnetic field can not produce significant heat for MNPs (where no coercivity H_c = 0 Oe) because of constant direction of applied magnetic field. MNPs with H_c = 0 Oe means no magnetization at 0 applied magnetic field. This suggests that MNPs are in superparamagnetic (in which spin relaxation is of 10^{-9} s). Measured time is 0.1–1 s in *DC* magnetic measurement, which can not recognize superparamagnetic spin relaxation. However, under AC magnetic field, direction of current changes over time. MNPs can change direction of magnetic spins with time. In general study, frequency (f) for direction change of current is 100–500 kHz.[37,40] Applied magnetic field up to 400 Oe.[37,40] Beyond this, polarization or dielectric effect will arise because permittivity is dependent of frequency (f) or permeability is dependent on magnetic field. This can cause many side effects in the body. The reciprocal value of frequency (f^{-1}) gives 2–10 × 10^{-6} s, which is assumed as the measured time (this value is close to superparamagnetic spin relaxation (10^{-9} s)). Thus, some magnetic moments could be recognized in AC magnetization.

Overall, the ferro-fluids undergo heat loss or power dissipation due to (1) hysteresis loss, (2) Brownian rotation loss, (3) Néels spin relaxation and (4) Eddy current (ED).[18]

Hysteresis loss in AC magnetic field is given by:

$$\text{Area} = f \int M \, dH \quad (6)$$

where f is the frequency of AC magnetic field and it is represented as $f = \omega/2\pi$, M magnetization, H applied magnetic field. The ratio of magnetisation M to the applied magnetic field H is defined as the susceptibility (χ). In AC field the susceptibility (χ) is expressed as real (χ') and imaginary (χ'') terms out of which the imaginary part is related to the heat dissipation of the system. Heat/power dissipation of the total system is expressed as:[18]

$$P = \mu_0 \pi \chi'' f {H_0}^2 \quad (7)$$

where μ_0 is the permeability of free space. The imaginary term is expressed as:

$$\chi'' = \frac{\omega\tau}{1 + (\omega\tau)^2}\chi \quad (8)$$

where τ is the total relaxation contributed by Brownian relaxation (τ_B) and Néel's relaxation (τ_N). In former the magnetic moment is aligned with the applied magnetic field (H) where particles rotates in AC field due to which collides with the surrounding medium and thus causes heating. While later relaxation is due to the magnetic spin domain rotation from 0–180°. Thus the combined relaxation is expressed as:

$$\frac{1}{\tau} = \frac{1}{\tau_B} + \frac{1}{\tau_N} \quad (9)$$

According to Faraday's and Lenz's law, the heat loss due to ED current is due to the interaction between the conductive material and oscillating magnetic field which can be represented as:

$$ED = \frac{(\mu\pi \, dfH_0)^2}{20\rho} \quad (10)$$

where μ is the permeability of a material, d, the diameter of the particle and ρ, resistivity of the material. These bi-functional nanocomposites are semiconductors/insulators, which have significantly high resistivity (ρ = ~10^2 Ohm cm). Thus the heat generation due to eddy current is negligible. For small particles where the particle size is less than that of the critical size (that is a single domain particle in size), the heating caused is mainly due to the contribution of Brownian and Néel's relaxations and some contribution from frequency, which can give hysteresis loss.

Heat-generation is dependent on frequency and applied magnetic field. The density of the particle relates the loss power density P with specific absorption rate (SAR) which can be calculated using following relation:[18]

$$\text{SAR} = c\frac{\Delta T}{\Delta t}\frac{1}{m_{magn}} \quad (11)$$

where c is the sample specific heat capacity, which is calculated by considering both sample weight and weight of water. Specific heat capacity of sample is neglected as its contribution is very small due to small weight. Thus the specific heat capacity of water is considered to represent the total heat capacity of the sample that is 4.18 J g^{-1} K^{-1}. $\Delta T/\Delta t$ is the slope of the time dependent temperature curve obtained at 400 A for 15 mg of the nanocomposite weight. m_{magn} is the amount of magnetite or Fe in the 1 ml system.

IV. Results and discussion

A. XRD study

The XRD patterns of YPO_4, YPO_4:5Eu, Fe_3O_4, and Fe_3O_4@YPO_4:5Eu nanoparticles capped with polyethylene glycol (PEG) are shown in Fig. 1(a). It is found that YPO_4 shows tetragonal structure having space group $I4_{1/amd}$ (JCPDS card no. 11-0254) and Fe_3O_4 shows face centered cubic structure with space group F_{d3m} (JCPDS card no. 19-0629). The broadening contribution from instrument (β_{inst}) is removed by using *Si* standard in XRD patterns.[40] YPO_4 shows a strong peak at (200) plane whereas Fe_3O_4 at (311) plane. Intensities of peaks corresponding to Fe_3O_4 decreases on coating its surface by YPO_4:5Eu. The lattice parameters, unit cell volume and average crystallite sizes of YPO_4, YPO_4:5Eu, Fe_3O_4 and Fe_3O_4@YPO_4:5Eu nanoparticles are given in Table 1. We used Scherrer's equation for calculating average crystallite sizes. Fig. S2 (see ESI†) shows the change in peak position of (200) plane of YPO_4 and YPO_4:5Eu nanoparticles. There is slight shift in peak position towards the lower 2θ by Eu^{3+} doping suggesting the substitution of Y^{3+} (1.01 Å) sites by Eu^{3+} (1.06 Å) ions. The crystallite size decreases from 32 to 22 nm due to the addition of 5 at% Eu^{3+} in YPO_4. Its *FWHM* increases from 0.22 to 0.27° in 2θ. However, we do not find any change in peak position of (311) plane Fe_3O_4 of due to the YPO_4:5Eu shell formation over Fe_3O_4 (core) and their crystallite sizes calculated from (311) plane are found to be in the range of 10 nm. Peaks corresponding to YPO_4:Eu could not be identified in Fe_3O_4@YPO_4:5Eu composites. This is related to the formation of small size particles of YPO_4:5Eu and the amorphous morphology because we did not heat sample after formation of composites.

Table 1 The lattice parameters (*a*, *c*), unit cell volumes (*V*) and crystallite sizes (*t*) of different samples

Sample	*a*, *c* (Å)	*V* (Å^3)	*t* (nm)
JCPDS: 11-0254	*a* = 6.904 *c* = 6.035	287.7	—
JCPDS: 19-0629	*a* = 8.396	591.9	—
YPO_4	*a* = 6.903(1) *c* = 6.032(1)	287.4(1)	32
YPO_4:5Eu	*a* = 6.910(1) *c* = 6.036(1)	288.2(1)	22
Fe_3O_4	*a* = 8.335(1)	579.0(1)	10
Fe_3O_4@YPO_4:5Eu	*a* = 8.327(1)	577.3(1)	10

B. TEM study

The TEM images of Fe_3O_4 and Fe_3O_4@YPO_4:Eu are shown in Fig. 2(a, c). The average particle size of the Fe_3O_4 was found to be ~10 nm. The selected area electron diffraction (SAED) study shows that the particles were crystalline with cubic structure (Fig. 2(b, d)). From the HRTEM it was found that the lattice spacing (d_{hkl}) of Fe_3O_4 is 2.52 Å (Fig. 2(e)) which matches with the (311) plane; whereas (d_{hkl}) for Fe_3O_4@YPO_4:5Eu was found to be 3.34 Å which is due to (200) plane (Fig. 2(f)). The size of the Fe_3O_4@YPO_4:5Eu was found to be 25 nm which is bigger than its counterpart crystallite size (10 nm) of Fe_3O_4 because of contribution of surface YPO_4:5Eu over core Fe_3O_4. The crystallite size determined is based on the XRD pattern of Fe_3O_4 whereas, the particle size determined is overall size of the composite. Usually, TEM particle size is more than the XRD crystallite size. The particles prepared are spherical and free from agglomeration.

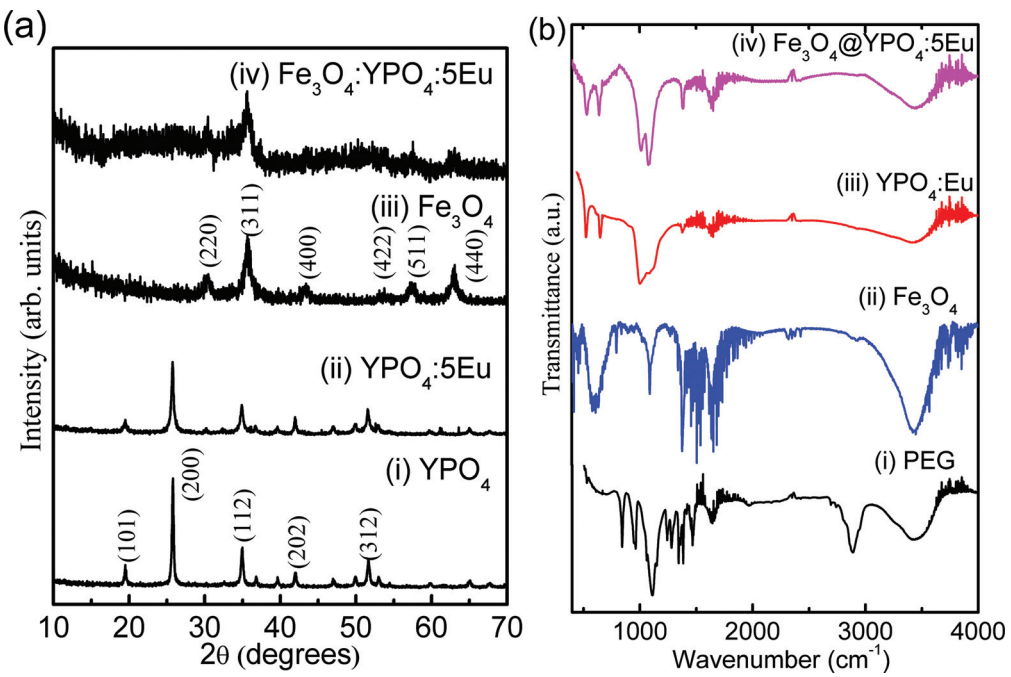

Fig. 1 (a) XRD patterns of YPO_4, YPO_4:5Eu, Fe_3O_4, and Fe_3O_4@YPO_4:5Eu and (b) FTIR spectra of PEG, Fe_3O_4, YPO_4:5Eu and Fe_3O_4@YPO_4:5Eu nanoparticles.

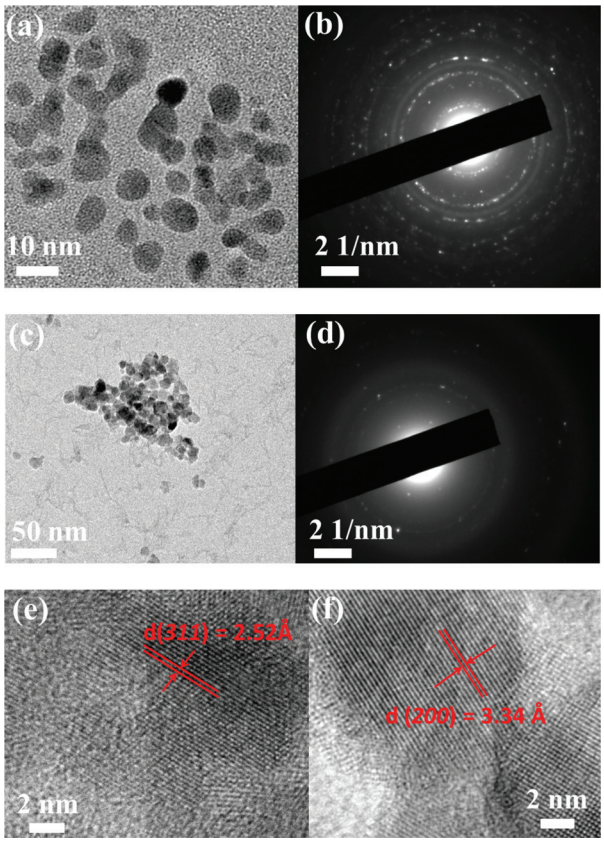

Fig. 2 TEM and SAED images of Fe_3O_4-MN (a, b) and Fe_3O_4@YPO_4:Eu (c, d) and their corresponding HRTEM (e, f), respectively.

C. FTIR study

Fig. 1(b) shows the FTIR spectra of PEG, Fe_3O_4, YPO_4:5Eu and Fe_3O_4@YPO_4:5Eu nanoparticles capped with PEG. The strong bands are observed at ~3430 and 1630 cm^{-1} which correspond to the stretching and bending vibrations of water (H_2O) present on the surface of the particles.[41] Pure PEG shows two bands at ~1076 cm^{-1} (*v-trans*) and 1110 cm^{-1} (*v-gauche*) which are assigned to C–O–C stretching vibrations (Fig. 1b(i)).[21] Fig. 1b(ii) shows a broad band at ~599 cm^{-1} which is assigned to Fe–O of Fe_3O_4 and two bands at 1092 and 1390 cm^{-1} correspond to S–O, which arises from $FeSO_4{\cdot}7H_2O$ used in synthesis.[18] IR spectra of YPO_4 and 5 at% Eu doped YPO_4 coated on Fe_3O_4 nanoparticles are shown in Fig. 1b(iii and iv). The typical peaks at ~525 and 650 cm^{-1} arise due to bending vibrations of $(PO_4)^{3-}$ (v_4 vibrations), whereas the strong bands at ~1002 and 1091 cm^{-1} merged together are assigned to stretching vibration of $(PO_4)^{3-}$ group (v_3 vibrations). Peaks corresponding to the stretching vibrations of H–C–H groups at ~2890 and 2950 cm^{-1} are also observed.[41] Fig. S3 (see ESI†) shows the comparison of IR spectra of YPO_4:Eu and Fe_3O_4@YPO_4:5Eu nanoparticles between 400–1400 cm^{-1} after background correction. This range shows the vibrational bands of PO_4 unit, where minimum four peaks could be observed. It is found that the ratio of intensities of v_3 to v_4 vibrations are found to be 3.2 and 5.6 for YPO_4:Eu and Fe_3O_4@YPO_4:5Eu nanoparticles, respectively. It is concluded that v_4 vibrations are most effective for Fe_3O_4@YPO_4:5Eu nanoparticles. Polarizability of PO_4 of YPO_4 changes after composite formation. There is chemical bonds between Fe_3O_4 and YPO_4:5Eu through possible bond (Fe···O–P).

D. Magnetization study

The magnetization (*M*) *vs.* applied magnetic field (*H*) data for the Fe_3O_4 and Fe_3O_4@YPO_4:5Eu (not shown). The magnetization values of Fe_3O_4 and Fe_3O_4@YPO_4:5Eu were found to be 47.5 and 11.1 emu g^{-1}, respectively at 2×10^{-4} Oe. The saturation magnetization of bulk Fe_3O_4 is 92 emu g^{-1},[42] which is much more than the prepared Fe_3O_4 and indicates that the particle size is less than bulk micron size particles. Here particle size (diameter, *D*) of prepared sample from TEM study is ~10 nm and its volume will be $4/3(\pi R^3)$, where *R* is radius of particle ($R = D/2$). At room temperature, thermal energy (kT = 0.03 eV) can overcome the particle/crystalline anisotropic energy (KV, *K* is the effective crystalline anisotropic constant and *V* is the particle volume). In a previous report, *K* for Fe_3O_4 MNPs is found to be 0.9×10^3 J m^{-3} at 300 K.[43] The KV is ~0.02 eV, which is close to the room temperature thermal energy (0.03 eV). In single domain particles, its magnetization vector tends to align along a particular direction called the easy direction. It gives the minimum magnetocrystalline anisotropy energy, which is an energy barrier of free rotation of magnetic moment away from easy direction/axis. When thermal energy overcomes, magnetization vector can rotate to opposite direction ($0 \rightarrow 180°$) within 10^{-8}–10^{-10} s. In such situation, particles exhibit superparamagnetic behaviour and relaxation is so fast compared to the measured time for VSM, up to 10^{-1} s. Domain rotation could not be detected by VSM at zero applied magnetic field. Net magnetization is zero at zero applied magnetic field. This is supported by the zero coercivity (H_c) value obtained in this study. When applied magnetic field increases, magnetization vector of domain will try to align towards the field direction, because thermal energy is dominated by applied magnetic field. The *M* values could be measured. With increase of *H*, *M* increases. The relation between thermal energy and particle energy is given in eqn (5).

E. Luminescence study

(i) Excitation study. Fig. 3(a) shows the excitation spectra of YPO_4:5Eu and Fe_3O_4@YPO_4:5Eu nanoparticles monitored at ~615 nm emission. A broad peak at ~250 nm is observed due to the Eu–O charge transfer band (CTB).[44] This arises due to the transition of 2p electrons of O^{2-} to the empty 4f orbitals of Eu^{3+} ions. Peaks at 315, 362, 376/382, 394 and 464 nm correspond to $^7F_{0,1} \rightarrow {}^5H_{3,6}$, $^7F_{0,1} \rightarrow {}^5D_0$, $^7F_{0,1} \rightarrow {}^5G_1$, $^5L_7$, $^7F_0 \rightarrow {}^5L_6$ and $^7F_{0,1} \rightarrow {}^5D_2$ transitions of Eu^{3+}, respectively.[44–46] The peak intensity at 394 nm is more than that of Eu–O charge transfer suggesting weak energy transfer from Eu–O to Eu^{3+}. In excitation spectra of Fe_3O_4@YPO_4:5Eu nanoparticles monitored at 615 nm emission, presence of Fe_3O_4 shows significant decrease in Eu–O charge transfer band intensity. Peak intensity at 394 nm also decreases significantly. There is evolution

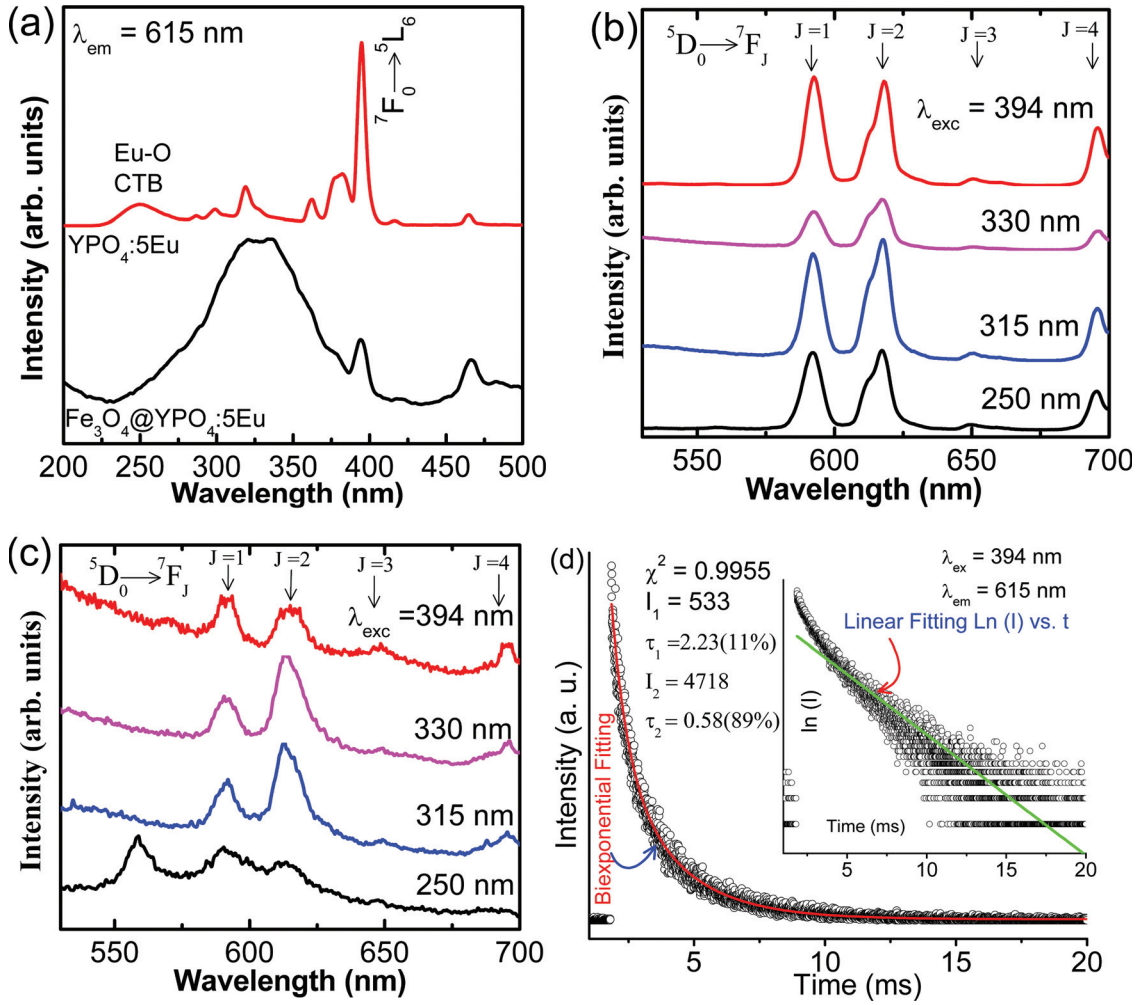

Fig. 3 (a) Excitation spectra of YPO_4:5Eu and Fe_3O_4@YPO_4:Eu. Emission spectra of YPO_4:5Eu (b) and Fe_3O_4@YPO_4:Eu (c) nanoparticles under 250, 315, 330 and 394 nm using xenon lamp as excitation source. (d) Decay spectra of 5 at% Eu^{3+} doped YPO_4 nanoparticles under 394 nm excitation and 615 nm emission. The inset of (d) shows the ln(*I*) *vs.* time, but there is no linear relationship indicating non-monoexponential decay.

of extra broad peak at 315–330 nm, which may be due to exciton formation when semiconductor/semimetal (*e.g.* Fe_3O_4) interfaces with another one insulator/semiconductor (YPO_4). Similar observations were reported in our recent studies (SnO_2:Eu@TiO_2, SnO_2:Eu@SiO_2, SnO_2:Eu@Y_2O_3).[47–49]

(ii) Emission study. Fig. 3(b and c) show the emission spectra of YPO_4:5Eu and Fe_3O_4@YPO_4:5Eu nanoparticles under 250, 315, 330 and 394 nm excitations. In Fig. 3(b) the emission spectrum of YPO_4:Eu shows peak of Eu^{3+} at 592 nm corresponding to the magnetic transition ($^5D_0 \rightarrow {}^7F_1$) along with peaks at 618 and 696 nm corresponding to electric dipole transition ($^5D_0 \rightarrow {}^7F_2$) and ($^5D_0 \rightarrow {}^7F_4$).[44,45] Apart from these prominent peaks, we could also observe other weak peaks centered at 650 nm corresponding to ($^5D_0 \rightarrow {}^7F_3$) transition. The luminescence intensity is more when excited at 394 nm in comparison with other three at 250, 315 and 300 nm. Fig. 3(c) shows the emission spectra of Fe_3O_4@YPO_4:5Eu nanoparticles under 250, 315, 330 and 394 nm excitations. On excitation at 330 nm it gives the maximum peak intensity whereas 394 nm excitation shows low intensity due to quenching of Eu^{3+} excited levels by Fe_3O_4.

Furthermore, in order to compare the difference in luminescence intensities at different excitation wavelengths, the integrated area under the curve is calculated for $^5D_0 \rightarrow {}^7F_1$ and $^5D_0 \rightarrow {}^7F_2$ transitions. All the fittings were carried out between 578 and 642 nm after removal of background. Luminescence intensity is more in the case of YPO_4:5Eu compared to that of Fe_3O_4@YPO_4:5Eu. This is because of the presence of the ferromagnetic impurity Fe_3O_4, which is a luminescence quencher. Table 2 gives parameters (peak position, FWHM of individual peak ($^5D_0 \rightarrow {}^7F_1$ and $^5D_0 \rightarrow {}^7F_2$ transitions) for YPO_4:5Eu and Fe_3O_4@YPO_4:5Eu when excited at 250, 315, 330 and 394 nm. Peak positions of $^5D_0 \rightarrow {}^7F_1$ are about 592 nm and those of $^5D_0 \rightarrow {}^7F_2$ are about 618 nm in case of YPO_4:5Eu in all excitations. Also, FWHM values for $^5D_0 \rightarrow {}^7F_1$ and $^5D_0 \rightarrow {}^7F_2$ are 8 and 10 nm, respectively. Whereas, peak positions of $^5D_0 \rightarrow {}^7F_1$ are about 590–592 nm and those of $^5D_0 \rightarrow {}^7F_2$ are about 611–615 nm in case of Fe_3O_4@YPO_4:5Eu in all excitations.

Table 2 Parameters obtained after integrated area calculation in luminescence spectra of samples: 5 at% Eu^{3+} doped YPO_4 nanoparticles (YPO_4:5Eu) and Fe_3O_4@YPO_4:5Eu under excitation at 250, 315, 330 and 394 nm. Asymmetric ratio (A_{21}) is intensity ratio of $^5D_0 \rightarrow {}^7F_2$ to $^5D_0 \rightarrow {}^7F_1$

Samples with corresponding parameters	Excitation at			
	250 nm	315 nm	330 nm	394 nm
YPO_4:5Eu				
Peak (nm) $^5D_0 \rightarrow {}^7F_1/{}^5D_0 \rightarrow {}^7F_2$	592/617.5	592/617.5	592/617	592.5/618
Width (nm)	8.5/10	8.0/9.5	8.5/10.0	7.5/8.5
A_{21}	1.2	1.3	1.7	1
Fe_3O_4@YPO_4:5Eu				
Peak (nm) $^5D_0 \rightarrow {}^7F_1/{}^5D_0 \rightarrow {}^7F_2$	590.5/611	592/613	590.5/613	589.5/615
Width (nm)	26/30.5	25/14	23/15	24.5/21
A_{21}	1	2.7	3.1	1.2

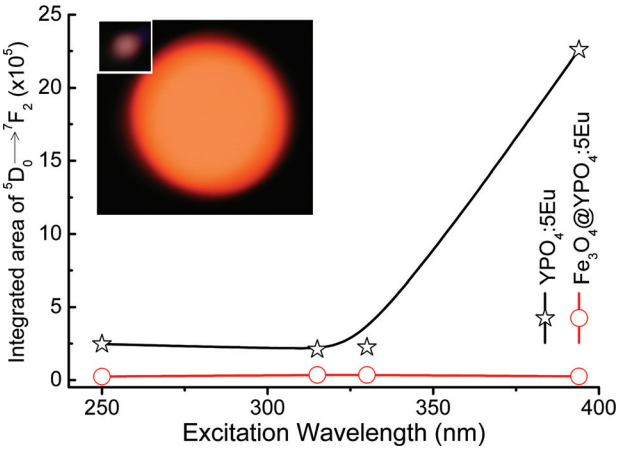

Fig. 4 Integrated area of $^5D_0 \rightarrow {}^7F_2$ transition obtained after different excitations at 250, 315, 330 and 394 nm. Inset shows the digital photograph the YPO_4:5Eu (larger) and Fe_3O_4@YPO_4:5Eu (smaller) nanoparticles under 266 nm laser excitation.

Also, FWHM values for $^5D_0 \rightarrow {}^7F_1$ and $^5D_0 \rightarrow {}^7F_2$ are 15–26 and 14–31 nm, respectively. Such large variation in values for different excitation peaks in wavelengths are related to interaction of EuO_8 with Fe_3O_4 or interaction of PO_4 group with Fe_3O_4, which was also observed by FTIR study. Local environment of EuO_8 is affected after Fe_3O_4 interaction.

The relative intensity ratio of electric dipole transition ($^5D_0 \rightarrow {}^7F_2$) to magnetic dipole transition ($^5D_0 \rightarrow {}^7F_1$) can be used as an effective parameter to understand the Eu^{3+} symmetry around the host lattice. This parameter is denoted by A_{21} called the asymmetric ratio.

$$A_{21} = \frac{\int_{603}^{642} I_2 \, d\lambda}{\int_{578}^{603} I_1 \, d\lambda} \quad (12)$$

where I_1 and I_2 represent the respective integrated intensities of ($^5D_0 \rightarrow {}^7F_1$) and ($^5D_0 \rightarrow {}^7F_2$) transitions of Eu^{3+}, respectively. A_{21} values are given in Table 2 for YPO_4:5Eu and Fe_3O_4@YPO_4:5Eu nanoparticles. The A_{21} values for YPO_4:5Eu are found to be 1.2, 1.3, 1.6 and 1.0, whereas for Fe_3O_4@YPO_4:5Eu values are found to be 1.0, 2.7, 3.1 and 1.2, under 250, 315, 330 and 394 nm excitation, respectively. This suggests the increase in asymmetric environment of EuO_8 after Fe_3O_4 covered with YPO_4:5Eu. Moreover, the comparison of integrated area of $^5D_0 \rightarrow {}^7F_2$ transition obtained after different excitations at 250, 315, 330 and 394 nm for YPO_4:5Eu and Fe_3O_4@YPO_4:5Eu nanoparticles are shown in Fig. 4. Inset of the Fig. 4 shows the digital photograph of the YPO_4:5Eu (larger) and Fe_3O_4@YPO_4:5Eu (smaller) nanoparticles under 266 nm laser excitation.

According to Judd–Ofelt theory the magnetic dipole transition is permitted one whereas the electric dipole transition is allowed exceptionally on condition that europium ions occupy site without inversion centre and sensitive to local symmetry.[30,50,51] When ΔJ = odd in f–f transition ($^{2S+1}L_J$* (excited state) → $^{2S+1}L_J$ (ground state)) is found to be odd, the transition is considered to be the magnetic dipole transition whereas it is electric dipole transition when ΔJ is even. The $J = L \pm S$ (L and S stand for orbital and spin quantum numbers, respectively). Since Eu^{3+} ions occupy asymmetry sites, it is expected that the intensities of electric dipole transition is more that of the magnetic dipole transition in all cases of $LnPO_4$:Eu^{3+}. In present case A_{21} is ~1 for YPO_4:5Eu nanoparticles on direct Eu^{3+} excitation at 394 nm whereas it increases to ~3 at 330 nm excitation for Fe_3O_4@YPO_4:5Eu.

(iii) Lifetime and quantum yield studies. Fig. 3(d) shows the luminescence decay for $^5D_0$ level of Eu^{3+} in YPO_4:5Eu nanoparticles. Excitation and emission wavelengths are fixed at 396 and 615 nm, respectively. The decay curve is fitted with bi-exponential function:

$$I = I_1 e^{(-t/\tau_1)} + I_2 e^{(-t/\tau_2)} \quad (13)$$

where I_0 is luminescence intensity at time (t = 0). I_1 and I_2 are the intensities at different time intervals and their lifetimes are τ_1 and τ_2, respectively. In TEM study, particle is found spherical in shape. This sphere can be divided into two equal volumes (*i.e.*, inner core covered with shell) and thus, the average lifetime τ_{av} can be calculated using eqn (14),[52]

$$\tau_{av} = \frac{I_1\tau_1^2 + I_2\tau_2^2}{I_1\tau_1 + I_2\tau_2}. \quad (14)$$

It gives τ_1 = 0.58 ms (89%) and τ_2 = 2.23 ms (11%) of which former is due to emission from surface Eu^{3+} and latter is because of the core Eu^{3+}. High contribution from surface is related to small size particle. Average lifetime (τ_{av}) is 1.1 ms.

The quantum yield study has been carried out on basis of absolute calculation. Detailed experimental information is given in the ESI† of our recent work.[53] In brief, 1–4 mg of sample is dispersed in 4 ml of ethanol solvent. The scattering intensity of solvent is taken after keeping excitation and emission wavelengths at same number 394 nm. This is referred to as $I_{solvent}$. Scattering intensity of sample dispersed in solvent is taken at the same parameters ($\lambda_{exc} = \lambda_{em}$ = 394 nm). This is taken as I_{sample}, where we choose wavelength at 394 nm

because of Eu^{3+} absorption. Emission intensity of dispersed sample/particles is recorded in 500–700 nm in which the emission peaks at 592 and 618 nm could be observed. This is referenced as $I_{emission}$. All experiments are performed in an integrated sphere, where sample/solvent is kept inside. The sphere has exit and entry of light and the angle between them is at 90° and inner surface is coated with $BaSO_4$. Since dispersed particles absorb light of 394 nm, only emitted light will be scattered from it. Difference in scattering light intensities ($I_{solvent} - I_{sample}$) will give the amount of light absorbed by the sample. The quantum yield (QY) is defined using eqn (15):

$$\Phi_{QY} = \frac{I_{emitted}}{I_{solvent} - I_{sample}}. \quad (15)$$

This is initially tested with a standard sample (Rhodamine G in ethanol/methanol). The emission quantum yield (QY) of YPO_4:5Eu was found to be 12%, which is close to the reported value $GdPO_4$:Eu sample (QY = 19%).[54]

(iv) Induction heating study. We have evaluated the heating ability of different magnetic particles with respect to their concentrations and magnetic fields/currents. The magnetic field produced from induction coil is directly dependent on the amount of current passing to the coil. Fig. 5(a, b) shows the heating temperature achieved by different concentrations of Fe_3O_4 and Fe_3O_4@YPO_4:5Eu at the applied current of 400 A with time up to 10 minutes. For all tested concentrations (2–20 mg), Fe_3O_4 can reach hyperthermia temperature that is ~40–43 °C even at lower concentrations (5 mg ml^{-1}) at 400 A of supplied current whereas Fe_3O_4@YPO_4:5Eu needs higher concentration to achieve hyperthermia temperature at around 10 mg ml^{-1}. All these samples are studied under the influence of magnetic field produced by 400 A of AC current. Fig. 5(c, d) shows the temperature achieved by Fe_3O_4 and Fe_3O_4@YPO_4:5Eu with time at different currents. Here concentration of the sample is 15 mg ml^{-1}. Inset of Fig. 5(c) shows the digital photograph of (i) Fe_3O_4@YPO_4:5Eu nanoparticles dispersed in water and (ii) same after magnetic field applied on it. Sample is highly dispersible in water, but after applying magnetic field, magnetic composites are attracted toward the magnetic field. The particles are studied using different currents varying in 200–400 A, out of which 400 A is found to be the more optimal as compared to that of the other currents.

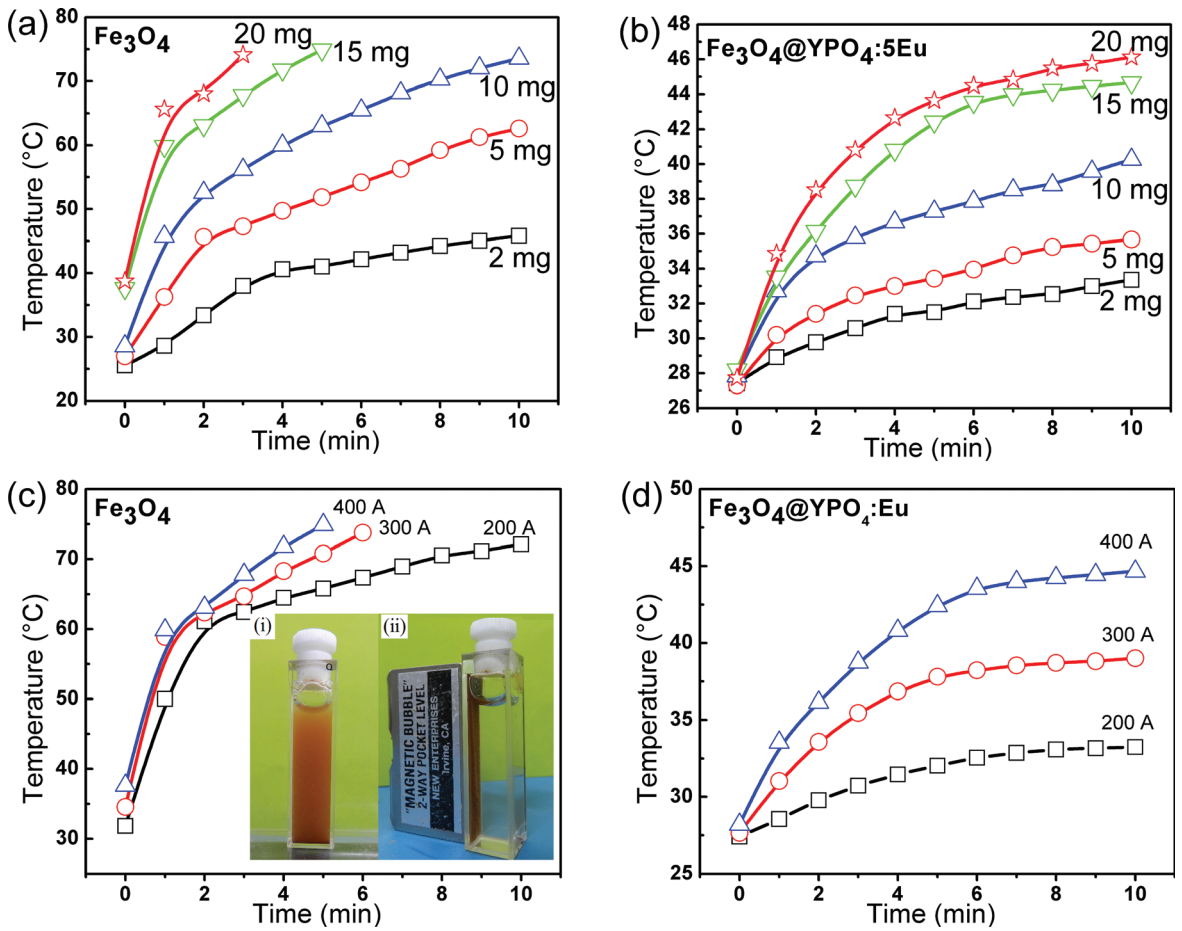

Fig. 5 The temperature achieved by (a) Fe_3O_4 and (b) Fe_3O_4@YPO_4:5Eu with time at different concentrations (current = 400 A and f = 265 kHz). The temperature achieved by (c) Fe_3O_4 and (d) Fe_3O_4@YPO_4:5Eu with time at different currents (concentration = 15 mg ml^{-1}). Inset of (c) shows the digital photograph of (i) Fe_3O_4@YPO_4:5Eu nanoparticles dispersed in water and (ii) same after magnetic field applied on it.

Table 3 SAR (W g^{-1}) values for Fe_3O_4 and Fe_3O_4@YPO_4:Eu magnetic nanoparticles at different currents

	SAR (W g^{-1})					
	Based on initial weight taken			Based on ICP-MS		
Samples (mg)	200 A	300 A	400 A	200 A	300 A	400 A
Fe_3O_4						
2	18	22	29	18	22	29
5	42	44	48	42	44	48
10	70	65	65	70	62	65
15	71	71	71	72	71	71
20	90	81	84	90	80	84
Fe_3O_4@YPO_4:Eu						
2	5	16	24	6	19	28
5	9	24	34	11	28	40
10	17	40	51	20	47	60
15	26	53	78	31	62	92
20	34	62	85	40	73	100

It is to be noted we did not pass current more than 400 A because a high current passing through coil yields heat at the coil, which is closed to the physiological temperature (37 °C) or above this. The calculated SAR values of Fe_3O_4 and Fe_3O_4@YPO_4:5Eu at different applied currents are given in Table 3. Recently, the SAR value ~92 W g^{-1} at 10 kA m^{-1} and 425 kHz and 33–38 W g^{-1} at 335 Oe (*i.e.*, 26.6 kA m^{-1}) and 265 kHz for Fe_3O_4 MNPs were reported.[18] Moreover, *Bovine serum albumin*-coated Fe_3O_4 nanoparticles are less toxicity and biocompatible.[55] These nanoparticles are effectively used in *in vivo* delivery applications.[56] Due to its quick heating ability, Fe_3O_4@YPO_4:5Eu nanoparticles can be effectively used in hypothermia applications. The toxicity and biocompatibility of the system will be investigated in a forth coming study.

F. Cellular uptake of the magnetic nanocomposites

For *in vitro* and *in vivo* hyperthermia and diagnostic applications, it is desirable that the nanocomposites show high internalization and accumulation in tumor cells. Hence, we have studied their interaction with mouse fibrosarcoma (Wehi 164) cells by Prussian blue staining and light microscopy. Without nanocomposites, there are no blue spots in Wehi 164 cells (Fig. 6(a)). The Wehi 164 cells treated with nanocomposites show the presence of a number of blue spots, indicating high intracellular uptake of nanocomposites by the tumor cells (Fig. 6(b)).

V. Conclusions

This study demonstrated the successful synthesis of Fe_3O_4@YPO_4:5Eu hybrid nanoparticles having both magnetic and luminescence characteristics. The as-prepared samples are characterized by XRD, FTIR, TEM/HRTEM, SAED, magnetisation, excitation, emission, lifetime and induction heating techniques. The average crystallite sizes calculated from XRD patterns are found to be ~22 and 10 nm for YPO_4:5Eu and Fe_3O_4@YPO_4:5Eu hybrid nanoparticles, respectively. This was also confirmed by TEM measurements. The emission peaks in the visible range from YPO_4:5Eu and Fe_3O_4@YPO_4:5Eu hybrid nanoparticles under 250, 315, 330 and 394 nm excitations are observed. Samples show strong emission under 330 nm excitation having average A_{21} = 1.7 and 3.1 for YPO_4:5Eu and Fe_3O_4@YPO_4:5Eu hybrid nanoparticles, respectively. The magnetization study of hybrid nanocomposites shows magnetization M_s = 11.1 emu g^{-1} (measured at 2×10^{-4} Oe) with zero coercivity. This is related to its superparamagnetic behaviour. Samples show high SAR values. The hyperthermia temperature can be attained under different applied magnetic fields/currents. Thus materials having both optical and magnetic properties can play an important role, such as tracers for biomedical applications along with hyperthermal action in cancer therapy. The Prussian blue staining signifies the cellular internalization of the magnetic nanoparticles in Wehi 164 cells by non specific endocytosis.

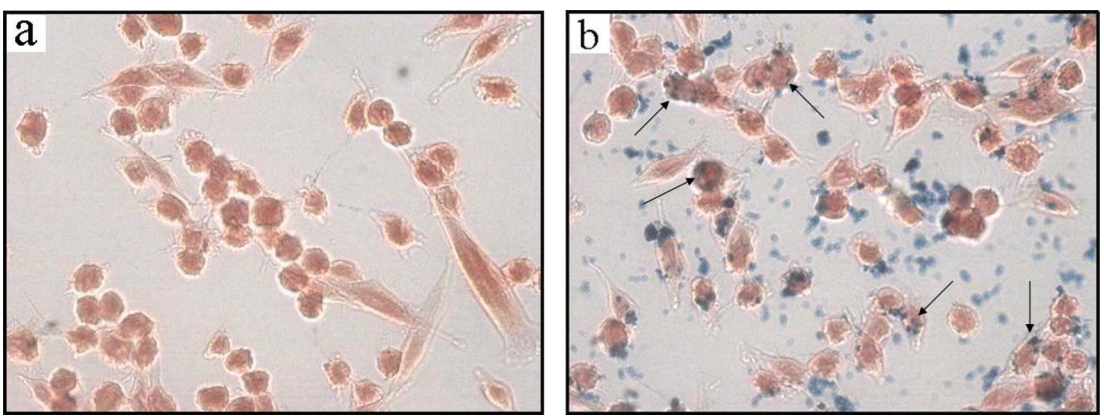

Fig. 6 Prussian blue staining of the Wehi 164 cells (a) control cell media without magnetic nanoparticles (b) cells treated with magnetic nanoparticles (0.5 mg ml^{-1}) for 6 h.

Acknowledgements

Authors thank Dr T. Mukherjee, Chemistry Group and Dr D. Das, Chemistry Division, BARC for the encouragement. A. K. Parchur acknowledges the financial support provided by University Grants Commission, Govt. of India through the Dr D. S. Kothari Post-Doctoral Fellowship. R. S. Ningthoujam thanks Dr P.V. Satyam, Institute of Physics, Sachivalaya Marg, Bhubaneswar-751005, India for providing TEM facility.

References

1 Z. Nie, A. Petukhova and E. Kumacheva, *Nat. Nanotechnol.*, 2010, **5**, 15.
2 R. B. Sim and R. Wallis, *Nat. Nanotechnol.*, 2011, **6**, 80.
3 Y. Tang and M. Ouyang, *Nat. Mater.*, 2007, **6**, 754.
4 (*a*) J. A. Scholl, A. L. Koh and J. A. Dionne, *Nature*, 2012, **483**, 421; (*b*) K. K. Haldar, T. Sen, S. Mandal and A. Patra, *ChemPhysChem*, 2012, **13**, 3989; (*c*) K. Ariga, A. Vinu, Y. Yamauchi, Q. Ji and J. P. Hill, *Bull. Chem. Soc. Jpn.*, 2012, **85**, 1.
5 C. Yang, G. Wang, Z. Lu, J. Sun, J. Zhuang and W. Yang, *J. Mater. Chem.*, 2005, **15**, 4252.
6 T. Bala, S. K. Arumugam, R. Pasricha, B. L. V. Prasad and M. Sastry, *J. Mater. Chem.*, 2004, **14**, 1057.
7 I. Ni, S. Yang, C. Jiang, C. Luo, W. Kuo, K. Lin and S. Tzeng, *J. Phys. Chem. C*, 2012, **116**, 8095.
8 A. A. Ansari, M. Alam, J. P. Labis, S. A. Alrokayan, G. Shafi, T. N. Hasan, N. A. Syed and A. A. Alshatwi, *J. Mater. Chem.*, 2011, **21**, 19310.
9 A. Kodiyan, E. A. Silva, J. Kim, M. Aizenberg and D. J. Mooney, *ACS Nano*, 2012, **6**, 4796.
10 C. Wu, J. Hong, X. Guo, C. Huang, J. Lai, J. Zheng, J. Chen, X. Mu and Y. Zhao, *Chem. Commun.*, 2008, 750.
11 X. Liu, P. K. Chu and C. Ding, *Mater. Sci. Eng., R*, 2010, **70**, 275.
12 H. Wang, Y. Sun, Y. Yu, J. Chen, R. Li, K. Cheng and Q. Chen, *Dalton Trans.*, 2012, **41**, 346.
13 H. Li, S. Gao, Z. Zheng and R. Cao, *Catal. Sci. Technol.*, 2011, **1**, 1194.
14 S. Zhou, Q. Chen, X. Hu and T. Zhao, *J. Mater. Chem.*, 2012, **22**, 8263.
15 J. Choi, J. C. Kim, Y. B. Lee, I. S. Kim, Y. K. Park and N. H. Hur, *Chem. Commun.*, 2007, 1644.
16 C. Zhong, P. Yang, X. Li, C. Li, D. Wang, S. Gai and J. Lin, *RSC Adv.*, 2012, **2**, 3194.
17 N. D. Thorat, K. P. Shinde, S. H. Pawar, K. C. Barick, C. A. Betty and R. S. Ningthoujam, *Dalton Trans.*, 2012, **41**, 3060.
18 R. Ghosh, L. Pradhan, Y. P. Devi, S. S. Meena, R. Tewari, A. Kumar, S. Sharma, N. S. Gajbhiye, R. K. Vatsa, B. N. Pandey and R. S. Ningthoujam, *J. Mater. Chem.*, 2011, **21**, 13388.
19 Z. Y. Ma, D. Dosev, M. Nichkova, S. J. Gee, B. D. Hammock and I. M. Kennedy, *J. Mater. Chem.*, 2009, **19**, 4695.
20 M. Yang, H. You, N. Guo, Y. Huang, Y. Zheng and H. Zhang, *CrystEngComm*, 2010, **12**, 4141.
21 (*a*) M. N. Luwang, R. S. Ningthoujam, Jagannath, S. K. Srivastava and R. K. Vatsa, *J. Am. Chem. Soc.*, 2010, **132**, 2759; (*b*) A. K. Parchur and R. S. Ningthoujam, *RSC Adv.*, 2012, **2**, 10854.
22 M. N. Luwang, R. S. Ningthoujam, S. K. Srivastava and R. K. Vatsa, *J. Am. Chem. Soc.*, 2011, **133**, 2998.
23 Q. Luo, S. Shen, G. Lu, X. Xiao, D. Mao and Y. Wang, *J. Mater. Chem.*, 2009, **19**, 8079.
24 S. Rodriguez-Liviano, F. J. Aparicio, T. C. Rojas, A. B. Hungría, L. E. Chinchilla and M. Ocaña, *Cryst. Growth Des.*, 2012, **12**, 635.
25 A. K. Parchur and R. S. Ningthoujam, *RSC Adv.*, 2012, **2**, 10859.
26 A. Kar and A. Patra, *Nanoscale*, 2012, **4**, 3608.
27 A. Kar, A. Datta and A. Patra, *J. Mater. Chem.*, 2010, **20**, 916.
28 V. M. Khot, A. B. Salunkhe, N. D. Thorat, R. S. Ningthoujam and S. H. Pawar, *Dalton Trans.*, 2013, **42**, 1249.
29 A. K. Parchur, A. I. Prasad, A. A. Ansari, S. B. Rai and R. S. Ningthoujam, *Dalton Trans.*, 2012, **41**, 11032.
30 R. S. Ningthoujam, *Enhancement of Photoluminescence by Rare Earth Ions Doping in Semiconductor Inorganic*, ed. S. B. Rai and Y. Dwivedi, Nova Science Publishers Inc, USA, 2012, ch. 6, pp. 145–182.
31 V. Skumryev, S. Stoyanov, Y. Zhang, G. Hadjipanayis, D. Givord and J. Nogués, *Nature*, 2003, **423**, 850.
32 Q. K. Ong, A. Wei and X. Lin, *Phys. Rev. B: Condens. Matter Mater. Phys.*, 2009, **80**, 134418.
33 S. Xuan, F. Wang, Y. J. Wang, J. C. Yu and K. C. Leung, *J. Mater. Chem.*, 2010, **20**, 5086.
34 C. Huang, K. Chuang, C. Chou, M. Wu, H. Sheu, D. Shieh, C. Tsai, C. Su, H. Lei and C. Yeh, *J. Mater. Chem.*, 2011, **21**, 7472.
35 C. Yang, J. Wu and Y. Hou, *Chem. Commun.*, 2011, **47**, 5130.
36 B. D. Cullity and C. D. Graham, *Introduction to Magnetic Materials*, John Wiley & Sons, Inc., Publication, Hoboken, New Jersey, 2nd edn, 2009.
37 R. S. Ningthoujam, R. K. Vatsa, A. Kumar and B. N. Pandey, *Functionalized Magnetic Nanoparticles: Concepts, Synthesis and Application in Cancer Hyperthermia*, ed. S. Banerjee and A. K. Tyagi, Elsevier Inc., USA, 2012, ch. 6, pp. 229–260.
38 A. Mukhopadhyay, N. Joshi, K. Chattopadhyay and G. De, *ACS Appl. Mater. Interfaces*, 2012, **4**, 142.
39 G. Wang and X. Su, *Analyst*, 2011, **136**, 1783.
40 A. K. Parchur and R. S. Ningthoujam, *Dalton Trans.*, 2011, **40**, 7590–7594.
41 A. K. Parchur, A. I. Prasad, S. B. Rai, R. Tewari, R. K. Sahu, G. S. Okram, R. A. Singh and R. S. Ningthoujam, *AIP Adv.*, 2012, **2**, 32119.
42 S. Cao, Y. Zhu and J. Chang, *New J. Chem.*, 2008, **32**, 1526.
43 S. Yoon and J. Korean, *Phys. Soc.*, 2011, **59**, 3069.
44 N. K. Sahu, R. S. Ningthoujam and D. Bahadur, *J. Appl. Phys.*, 2012, **112**, 014306.

45 A. K. Parchur, R. S. Ningthoujam, S. B. Rai, G. S. Okram, R. A. Singh, M. Tyagi, S. C. Gadkari, R. Tewari and R. K. Vatsa, *Dalton Trans.*, 2011, **40**, 7595.
46 G. S. R. Raju, E. Pavitra, Y. H. Ko and J. S. Yu, *J. Mater. Chem.*, 2012, **22**, 15562.
47 R. S. Ningthoujam, V. Sudarsan, S. V. Godbole, L. Kienle, S. K. Kulshreshtha and A. K. Tyagi, *Appl. Phys. Lett.*, 2007, **90**, 173113.
48 R. S. Ningthoujam, V. Sudarsan and S. K. Kulshreshtha, *J. Lumin.*, 2007, **127**, 747.
49 R. S. Ningthoujam, *Chem. Phys. Lett.*, 2010, **497**, 208.
50 B. R. Judd, *Phys. Rev.*, 1962, **127**, 750.
51 G. S. Ofelt, *J. Chem. Phys.*, 1962, **37**, 511.
52 N. S. Singh, R. S. Ningthoujam, N. Yaiphaba, S. D. Singh and R. K. Vatsa, *J. Appl. Phys.*, 2009, **105**, 064303.
53 N. S. Singh, R. S. Ningthoujam, M. N. Luwang, S. D. Singh and R. K. Vatsa, *Chem. Phys. Lett.*, 2009, **480**, 237.
54 N. Yaiphaba, R. S. Ningthoujam, N. S. Singh, R. K. Vatsa, N. R. Singh, S. Dhara, N. L. Misra and R. Tewari, *J. Appl. Phys.*, 2010, **107**, 034301.
55 A. Bajaj, B. Samanta, H. Yan, D. J. Jerry and V. M. Rotello, *J. Mater. Chem.*, 2009, **19**, 6328.
56 B. Samanta, H. Yan, N. O. Fischer, J. Shi, D. J. Jerry and V. M. Rotello, *J. Mater. Chem.*, 2008, **18**, 1204.

